

impact can be derived from the relative brightness of the surrounding terrain observed by both NIR2 and Diviner (17). Model cooling curves for $E_h = 5\%$ (Fig. 2) show that a regolith ice mass fraction of $>2\%$ is required to reproduce this behavior for the assumed regolith properties.

Finally, a layer of a few millimeters thick heated to an initial temperature of ~ 1000 K is consistent with both the Diviner data and the dynamics of the hydrogen vapor cloud observed by LAMP (18). At these temperatures, the regolith is desiccated nearly instantaneously, but a more gradual flux of sublimed water molecules continues as the thermal wave propagates downward. The above models imply that this gradual process accounts for $\sim 30\%$ of water molecules sublimed within the impact zone over the course of 4 min. For a heated area of 30 to 200 m^2 and ice mass fractions of 1%, 10%, and 22% (filled pores), instantaneous and gradual sublimation produce a total of 3 to 20 kg, 20 to 130 kg, and 50 to 300 kg of water vapor, respectively. This range is comparable to the ~ 155 kg of water vapor observed by LCROSS during this period (1). Thus, a substantial portion of the observed water vapor may have been supplied by the steaming crater.

References and Notes

1. A. Colaprete *et al.*, *Science* **330**, 463 (2010).
2. D. A. Paige *et al.*, *Science* **330**, 479 (2010).
3. K. Watson, B. C. Murray, H. Brown, *J. Geophys. Res.* **66**, 3033 (1961).
4. J. A. Zhang, D. A. Paige, *Geophys. Res. Lett.* **36**, L16203 (2009).

5. D. A. Paige *et al.*, *Space Sci. Rev.* **150**, 125 (2010).
6. See supporting material on Science Online.
7. Optical depth was calculated from the difference in counts between the T+90s orbit and the average of the T-2h and T+2h orbits (6), converted to radiance using a factor of $3.9 (\pm 10\%) \times 10^{-3} W m^{-2} sr^{-1} counts^{-1}$. Assuming single scattering, the total normal optical depth is $\tau = (4\pi\mu)/(F\varpi_0P)$, where l is the measured radiance enhancement, μ is the emission angle cosine, F is the solar irradiance within the pass band ($1130 W m^{-2}$), $\varpi_0 \approx 0.34$ is the single-scattering albedo, and $P \approx 0.38$ is the scattering phase function for lunar soil (8). The measurement error in the solar channel is estimated to be ~ 2 counts, giving an uncertainty of 2.8 counts ($\sim 0.01 W m^{-2} sr^{-1}$) in the difference.
8. E. J. Foote *et al.*, *40th Lunar Planet. Sci. Conf.*, abstract 2500 (2009).
9. W. D. Carrier, *Moon* **6**, 250 (1973).
10. We calculated the second and third moments of a lunar soil size distribution (9), giving corresponding radii $r_2 \approx 13 \mu m$ (cross section-weighted mean) and $r_3 \approx 16 \mu m$ (volume-weighted mean). The column mass ($kg m^{-2}$) was then calculated according to $\mu = \frac{4}{3}\pi\rho r_3^3 \cdot N = \frac{4}{3}\rho r_3^3 \tau / Q_{ext} r_2^2$, where $\rho = 3600 kg m^{-3}$ is the density of individual grains, τ is the visible optical depth, and $Q_{ext} = 2.0$ is the optical extinction efficiency.
11. G. V. Belyakov *et al.*, *Combust. Explos. Shock Waves* **13**, 524 (1977).
12. P. H. Schultz *et al.*, *Science* **330**, 468 (2010).
13. The ranges account for the combined 1σ measurement error in all channels due to instrument noise, data misregistration, background variability, and field-of-view effects (6).
14. The 1D thermal model is based on that of Vasavada *et al.* (19) and includes vertical conduction and surface emission as well as temperature-dependent thermal conductivities and heat capacities. Our ice sublimation and vapor diffusion model is based on that of Fanale and Salvail (20) for comets, where we have adapted the thermal model to adjust thermophysical properties according to local ice content. Unless otherwise

- indicated, we assume a porosity of 50%, mean grain separation of 70 μm , and infrared emissivity of 0.95.
15. D. Braslau, *J. Geophys. Res.* **75**, 3987 (1970).
 16. D. E. Rehfuss, *Moon* **11**, 19 (1974).
 17. Topographic features illuminated by indirect sunlight around the shadowed impact site cannot be clearly seen in Diviner's pre-impact solar channel data, although these features are observed by the LCROSS near-infrared camera (NIR2) (22). Because the indirect sunlight signal is below Diviner's noise level of 2 counts in the solar channel, the upper limit of this signal is $\sim 2\times$ the gain factor, or $I_{Div} = 7.8 \times 10^{-3} W m^{-2} sr^{-1}$. The radiance actually observed by NIR2 for such a signal is less than $I_{NIR} = (I_{Div}/F_{Div}) \cdot F_{NIR}$, where F is the solar irradiance at the Moon for the given pass band. Although the value of F_{NIR} is unknown, we estimate it to be 130 $W m^{-2}$, assuming 80% sensitivity from 1000 to 1700 nm and zero sensitivity outside this range (21). Again using $F_{Div} = 1130 W m^{-2}$, this yields $I_{NIR} = 0.9 \times 10^{-3} W m^{-2} sr^{-1}$. Setting this equal to the equivalent blackbody radiance for the same pass band gives a value of ~ 410 K as a conservative estimate of NIR2's minimum detectable temperature.
 18. G. R. Gladstone *et al.*, *Science* **330**, 472 (2010).
 19. A. R. Vasavada, D. A. Paige, S. Wood, *Icarus* **141**, 179 (1999).
 20. F. P. Fanale, J. R. Salvail, *Icarus* **60**, 476 (1984).
 21. Goodrich SU320KTX-1.7RT (spec sheet, www.sensorsinc.com/downloads/SU320KTX.pdf).
 22. Some of the research described in this paper was carried out at the Jet Propulsion Laboratory, California Institute of Technology, under a contract with NASA.

Supporting Online Material

www.sciencemag.org/cgi/content/full/330/6003/477/DC1
Materials and Methods
Figs. S1 to S8
Table S1
References

30 August 2010; accepted 22 September 2010
10.1126/science.1197135

Diviner Lunar Radiometer Observations of Cold Traps in the Moon's South Polar Region

David A. Paige,^{1*} Matthew A. Siegler,¹ Jo Ann Zhang,¹ Paul O. Hayne,¹ Emily J. Foote,¹ Kristen A. Bennett,¹ Ashwin R. Vasavada,² Benjamin T. Greenhagen,² John T. Schofield,² Daniel J. McCleese,² Marc C. Foote,² Eric DeJong,² Bruce G. Bills,² Wayne Hartford,² Bruce C. Murray,³ Carlton C. Allen,⁴ Kelly Snook,⁵ Laurence A. Soderblom,⁶ Simon Calcutt,⁷ Fredric W. Taylor,⁷ Neil E. Bowles,⁷ Joshua L. Bandfield,⁸ Richard Elphic,⁹ Rebecca Ghent,¹⁰ Timothy D. Glotch,¹¹ Michael B. Wyatt,¹² Paul G. Lucey¹³

Diviner Lunar Radiometer Experiment surface-temperature maps reveal the existence of widespread surface and near-surface cryogenic regions that extend beyond the boundaries of persistent shadow. The Lunar Crater Observation and Sensing Satellite (LCROSS) struck one of the coldest of these regions, where subsurface temperatures are estimated to be 38 kelvin. Large areas of the lunar polar regions are currently cold enough to cold-trap water ice as well as a range of both more volatile and less volatile species. The diverse mixture of water and high-volatility compounds detected in the LCROSS ejecta plume is strong evidence for the impact delivery and cold-trapping of volatiles derived from primitive outer solar system bodies.

The Moon's polar regions are notable because of their potential to cryogenically trap water ice and other volatile species (1). The Lunar Reconnaissance Orbiter (2) (LRO) Diviner Lunar Radiometer Experiment has been mapping the infrared emission from the Moon

since July 2009 using seven spectral channels that span a wavelength range from 7.55 to 400 μm at a spatial resolution of ~ 200 m (3). Thermal maps of the south polar region (Fig. 1, A and B) were obtained during the LRO monthly mapping cycle just before the Lunar Crater Observation and Sensing

Satellite (LCROSS) impact (4), as the Moon approached southern summer solstice (5). The mapped quantity is the bolometric brightness temperature, which is the wavelength-integrated radiance in all seven Diviner channels expressed as the temperature of an equivalent blackbody (6). For quantifying the overall heat balance of the surface and comparing with available models, the bolometric brightness temperature is the most fundamental and interpretable measurable quantity. For the simplest case in which Diviner's surface footprint is filled with a blackbody of uniform surface temperature, the bolometric brightness temperature will be equal to the temperature of the surface. In the more general case, where Diviner's surface

¹Department of Earth and Space Sciences, University of California, Los Angeles, 595 Charles E. Young Drive East, Los Angeles, CA 90095, USA. ²Jet Propulsion Laboratory, California Institute of Technology, Pasadena, CA 91109, USA. ³California Institute of Technology, Pasadena, CA 90025, USA. ⁴NASA Johnson Space Center, Houston, TX 77058, USA. ⁵NASA Goddard Space Flight Center, Greenbelt, MD 20771, USA. ⁶U.S. Geological Survey, Flagstaff, AZ 86001, USA. ⁷Oxford University, Oxford OX1 3PU, UK. ⁸University of Washington, Seattle, WA 98195, USA. ⁹NASA Ames Research Center, Moffett Field, CA 94035, USA. ¹⁰University of Toronto, Toronto, ON M5S 3B1, Canada. ¹¹State University of New York, Stony Brook, NY 11794, USA. ¹²Brown University, Providence, RI 02912, USA. ¹³University of Hawaii, Honolulu, HI 96822, USA.

*To whom correspondence should be addressed. E-mail: dap@moon.ucla.edu

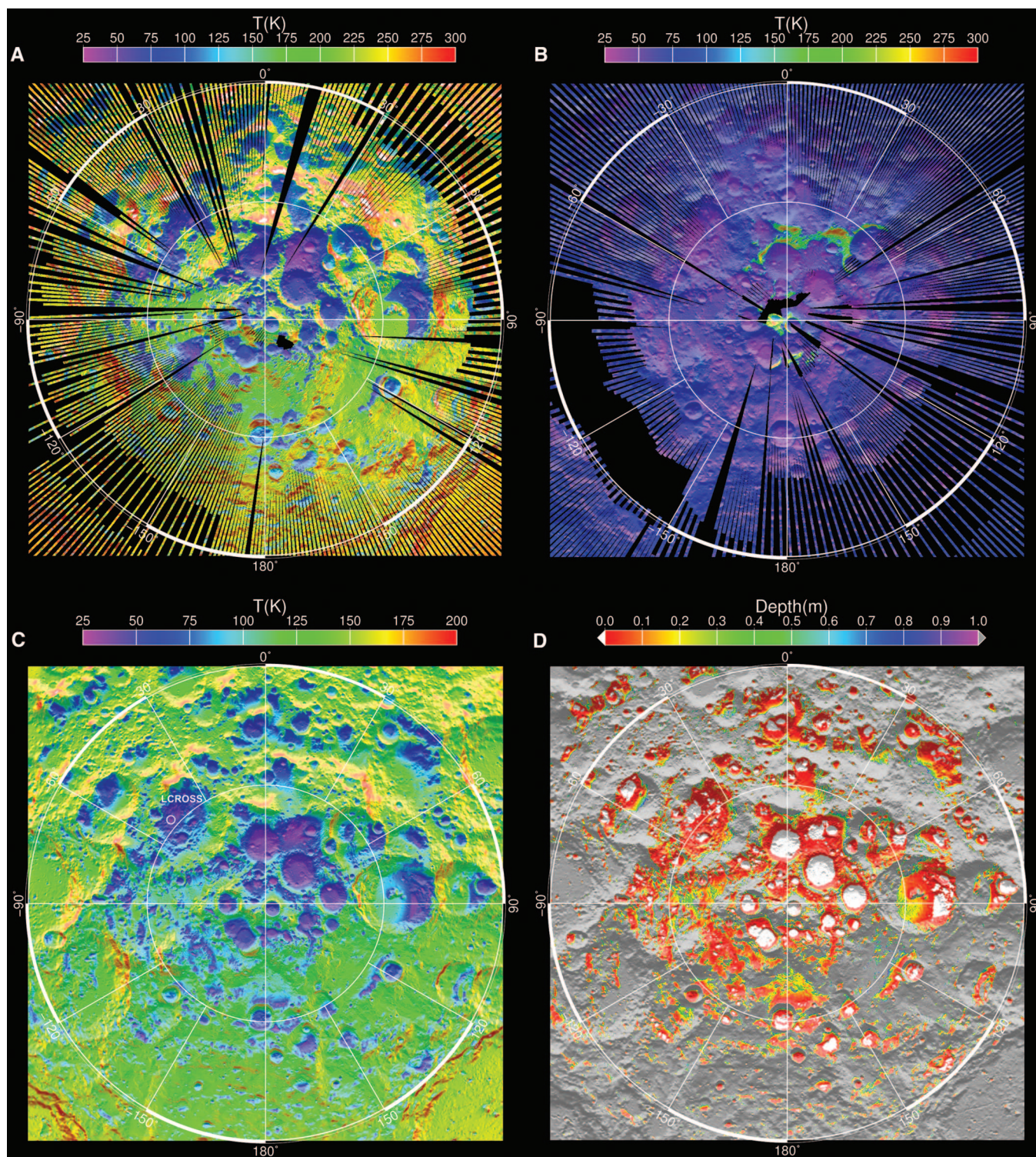


Fig. 1. Maps of measured and model-calculated surface and subsurface temperatures in the lunar south polar region. The outer circle on all maps is 80° south latitude. Observations were acquired between 6 September and 3 October 2009 as the Moon approached southern summer solstice. **(A)** Diviner-measured daytime bolometric brightness temperatures acquired between 11.4 and 13.6 hours local time (5). **(B)** Diviner-measured nighttime bolometric brightness temperatures acquired between 21.41 and 1.66 hours local time (5). **(C)** Model-calculated annual average near-

surface temperatures and the location of the LCROSS impact in Cabeus Crater. **(D)** Model-calculated depths at which water ice would be lost to sublimation at a rate of less than 1 kg m^{-2} per billion years. The white regions define the locations where water ice can currently be cold trapped on the surface, the colored regions define the upper surface of the lunar ice permafrost boundary, and the gray regions define locations where subsurface temperatures are too warm to permit the cold-trapping of water ice within 1 m of the surface. High-resolution images are available in the SOM.

footprint contains small-scale slopes, shadows, or rocks, the brightness temperatures in Diviner's individual infrared channels may vary with wavelength depending on the distribution of sub-footprint-scale temperatures, spectral emissivities, and photometric properties. In this case, the bolometric brightness temperature cannot be interpreted in terms of a unique surface temperature. However, within cold regions that are not in direct sunlight, simultaneously acquired brightness temperatures in Diviner channels 7 (25 to 41 μm), 8 (50 to 100 μm), and 9 (100 to 400 μm) are in good agreement (6), which is consistent with uniformly high spectral emissivity across this wavelength range and relatively uniform temperatures within each Diviner footprint (fig. S1, A and B). This interpretation is supported by the results of an analysis of data acquired in each of the Diviner infrared channels at the LCROSS impact site in Cabeus Crater (7). For unilluminated regions, we use Diviner bolometric brightness temperatures as reasonably accurate proxies for the temperature of the surface.

The thermal maps show that the coldest regions are located on the floors of larger impact craters that receive no direct sunlight (Fig. 1, A and B). For these regions, previous modeling studies have shown that the main heat source is emitted infrared radiation from distant interior sunlit crater walls (8–11). Topographic relief within cold crater floor regions can provide additional radiation shielding, resulting in intensely cold localized regions with measured mid-day bolometric brightness temperatures as low as 29 K. Heat flow from the lunar interior may contribute to the overall heat balance of these coldest surfaces, but is not dominant compared to heating from scattered solar and infrared radiation during this season (6).

Diviner's summer solstice observations represent a valuable snapshot of the south polar region surface temperatures that can be extended in depth and in time with models. We have developed a thermal model that realistically accounts for the effects of large-scale topographic relief on direct and indirect solar and infrared radiation on

the heat balance of the lunar surface (6). The model uses a $\sim 500\text{-m}$ -scale triangular mesh based on south polar topography derived from the Kaguya LALT laser altimeter (12) and a spatially uniform set of thermal and reflectance parameters that are generally consistent with those derived from previous studies (6). The excellent overall agreement between maps (fig. S3, A and B) and histograms (Fig. 2A) of the observed and calculated bolometric temperatures demonstrate the general validity of our modeling approach. The only notable discrepancy occurs for daytime temperatures in the shadowed portions of craters that have measured bolometric temperatures in the range of 60 to 120 K, where the model underestimates temperatures by roughly 15 K (fig. S4, A and B). This may be largely due to directionally anisotropic infrared emission from rough sunlit crater walls, which is not accounted for in the present model (6). Given the better agreement between the model and the Diviner nighttime data, we estimate that the net effect on model-calculated annual average temperatures at 2-cm depth (Figs. 1C and 2B) is less than 7 K in the warmest craters and close to zero in the coldest craters. For the limiting case of zero heat flow from the lunar interior, the temperatures at greater depths would be close to this near-surface average temperature (11). However, with non-zero heat flow, average temperatures will increase with depth at a rate proportional to the heat flow rate and inversely proportional to the thermal conductivity. Using parameters derived from the heat flow experiments at the Apollo 15 and 17 landing sites (13), we estimate that LCROSS impact site temperatures at 2-m depth should be <6 K higher than annual average surface temperatures (fig. S5). Although the Diviner bolometric temperatures presented here and cooling curves at the LCROSS impact site are generally consistent with the presence of unconsolidated regolith near the surface (7, 14), the thermophysical properties of the Moon's cryogenic regolith are not currently well constrained and could differ substantially from those in warmer regions (15), particularly at depth. We expect that the Moon's cryogenic regions extend to depths of at least tens of meters below the surface, but estimating the volumetric extent of the Moon's cryogenic regions purely from surface-temperature observations is highly uncertain.

Thermal model results can be used to estimate the stability of water ice deposits to loss by sublimation and diffusive migration through the lunar regolith (11, 16). Figure 1D shows a map of the depths at which water ice would be lost at a rate of less than 1 kg m^{-2} per billion years, which corresponds to a loss rate of 1 mm per billion years for a pure ice deposit (6). The results show that surface cold traps for water ice are surrounded by much more extensive "lunar permafrost" regions where water ice is stable in close proximity to the surface (17). These regions may receive direct solar radiation during periods when solar lighting conditions are most favorable, but maintain

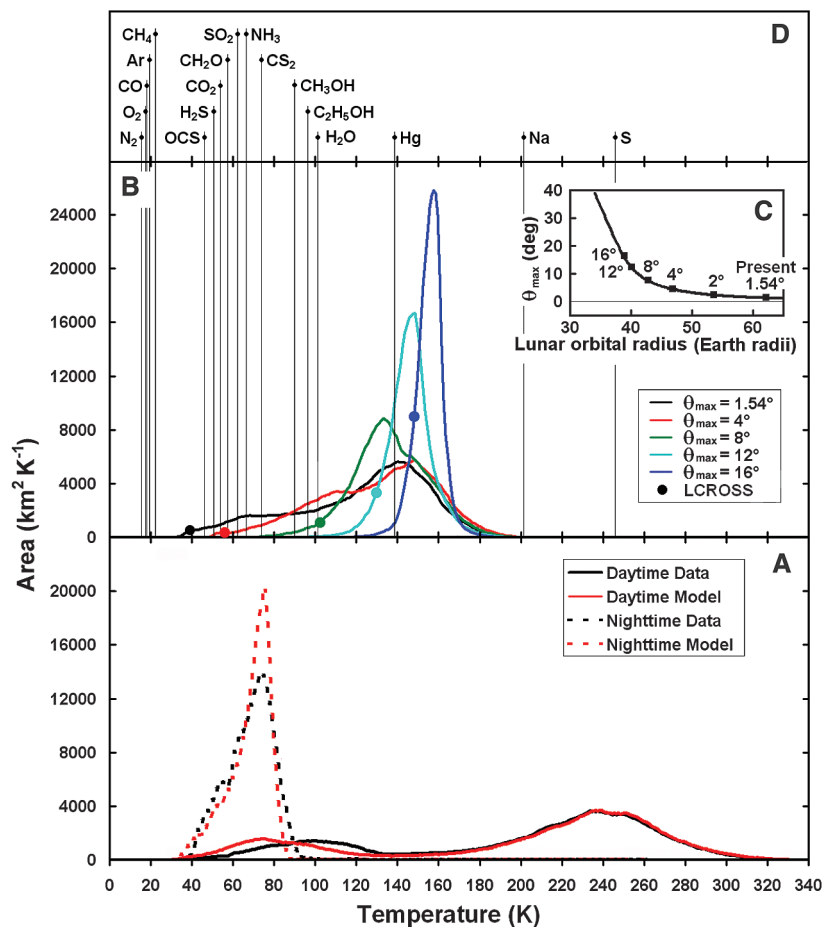


Fig. 2. (A) Normalized histograms of measured daytime and nighttime bolometric brightness temperatures for the maps shown in Fig. 1, A and B, with comparisons to model-calculated surface temperatures at the same locations and times as those of the Diviner observations (fig. S3, A and B). (B) Histograms of model-calculated annual average temperatures at 2-cm depth for the maps shown in Fig. 1C and fig. S7, A to D, and at the LCROSS impact site for selected values of θ_{max} , the mean maximum angle between the Moon's spin axis and the normal to the ecliptic plane. $\theta_{\text{max}} = 1.54^\circ$ for present-day conditions. (C) The recent evolution of θ_{max} as a function of the Earth-Moon distance (29). (D) The volatility temperatures of a range of potential cold-trapped volatile compounds (21, 22).

annual maximum temperatures at depth that are sufficiently cold to effectively prevent appreciable water loss due to sublimation. Because of their more hospitable surface thermal and illumination environments, lunar permafrost regions may be accessible locations for future in situ exploration of the Moon's cold traps.

The overall picture painted by the present thermal state of the lunar south polar region is one of extreme cold. Temperatures in the Moon's larger cold traps are closer to those expected for the poles of Pluto (18) than for Earth's closest neighbor. At the cold temperatures that exist within most south polar craters, cold-trapped water molecules have negligible mobility (16), such that any water molecules deposited on the surface will not effectively diffuse below the surface where they can be protected from loss processes such as photolysis and sputtering (19). In cryogenic regions, burial of frozen volatiles by impact gardening is likely to be a much more effective process (20). However, warmer permafrost regions that currently exist at the margins of cold traps may represent somewhat more favorable environments for the downward diffusion of water molecules into the regolith, which should be aided by the daytime temperature gradient between warmer surface layers and colder subsurface layers below.

The distribution of temperatures in the lunar south polar region also places constraints on the thermal stability of nonwater volatile species. Figure 2D shows the volatility temperatures (the temperatures at which pure solids exposed to vacuum at the surface would sublimate at a rate of 1 mm per billion years) for several volatile species (21, 22). Nonwater subsurface volatiles will also be stable to sublimation at higher temperatures owing to the effects of diffusive migration through the regolith (6). Large areas of the lunar south polar region have the capability to cold-trap water and less volatile species such as mercury and sodium. All three of these volatile species were in the LCROSS ejecta plume (4, 14, 23). Colder surface and subsurface areas in the south polar region also have the capability to cold-trap so-called super volatile species that have higher volatility than water, which include compounds such as sulfur dioxide, carbon dioxide, formaldehyde, ammonia, and methanol. The detection of a representative cross-section of these same supervolatile species in the LCROSS ejecta plume (4) represents strong evidence for the impact delivery of volatiles to the Moon by primitive outer solar system bodies, and the subsequent cold-trapping of these volatiles at the lunar poles (21, 22).

A question of interest regarding the lunar cold traps is whether they contain abundant deposits of nearly pure water ice such as those discovered by radar observations of impact craters at the poles of Mercury (24). Diviner-measured summer solstice daytime and nighttime surface bolometric brightness temperatures of 46.7 and 38.7 K in the region surrounding the LCROSS impact

site, and model-calculated annual average temperatures at this site at a depth of 2 cm, are close to 38 K (6). As shown in Figs. 1, C and D, and 2B, the LCROSS impact site is a surface cold trap for water and is among the coldest locations in the south polar region. The Lunar Prospector Neutron Spectrometer (LPNS) results show that the average hydrogen abundance in the near-surface regolith at the south pole is ~70 parts per million (ppm) by weight, which translates to a water-equivalent average abundance of ~600 ppm by weight (25). Our results show that the surface and near-surface water ice cold traps comprise >66% of the surface area poleward of 85° south latitude (Fig. 1D). If we assume that all the hydrogen detected by LPNS was uniformly distributed within these cold traps, then the average water-equivalent abundance would be only ~1000 ppm by weight, which is substantially less than the 1 to 10% water content inferred at the LCROSS impact site (4). This suggests that the LCROSS site must be enriched in water compared to the average south polar near-surface cold trap, which is consistent with enhanced hydrogen abundances observed in the Cabeus region by orbital neutron spectrometers (26–28).

The spin pole of the Moon is currently in a tidally damped Cassini State 2 configuration in which the time-averaged maximum angle between the Moon's spin axis and the normal to the ecliptic plane (θ_{\max}) has decreased to its present value of $\theta_{\max} = 1.54^\circ$ as the Earth-Moon distance increased over time (Fig. 2C) (29). The absolute time scale for the tidal evolution of the Earth-Moon system is highly uncertain, but it is likely that the transition depicted in Fig. 2C has occurred over a period of more than 1 billion years (30). Model-calculated annual average near-surface temperatures $\theta_{\max} = 4^\circ, 8^\circ, 12^\circ,$ and 16° (Fig. 2B and fig. S7, A to D) show that portions of the Moon's south polar region cooled considerably as the Moon's orbital radius increased, first creating cold traps capable of cold-trapping water, and then trapping compounds with higher volatility. The LCROSS impact site, which is located on the floor of the large Cabeus impact crater, is typical of the coldest areas on the Moon today. However, earlier in the Moon's orbital history, when θ_{\max} was greater than $\sim 10^\circ$, the floors of large-impact craters were not the coldest areas on the Moon because the walls of these relatively shallow craters did not shield their floors from direct solar radiation. Based on the results in Fig. 2B and fig. S7, A to D, the Moon's earliest surviving near-surface cold traps are not located on the floors of large-impact craters, but rather on the floors of intermediate-sized craters, which thus may have had longer opportunities to accumulate water ice.

References and Notes

1. K. Watson, B. C. Murray, H. Brown, *J. Geophys. Res.* **66**, 3033 (1961).
2. G. Chin *et al.*, *Space Sci. Rev.* **129**, 391 (2007).
3. D. A. Paige *et al.*, *Space Sci. Rev.* **150**, 125 (2010).

4. A. Colaprete *et al.*, *Science* **330**, 463 (2010).
5. The LRO orbit plane is inclined 90° to the lunar equator and is fixed in inertial space. LRO's ground track rotates through 360° of longitude every sidereal month, allowing Diviner to make one daytime and one nighttime map every 27.3-day mapping cycle in pushbroom nadir mapping mode. Local time on the Moon can be expressed in hours by normalizing the angular distance between geographic longitude and the longitude of the solar point to a 24-hour day. We define daytime to be between 6 a.m. and 6 p.m. local time, and nighttime to be between 6 p.m. and 6 a.m. local time. Because the plane of the LRO orbit rotates relative to the lunar terminator by 360° every Earth year, the local times of Diviner's observations drift by ~ 2 hours during each mapping cycle. The subsolar latitude on the Moon currently varies by approximately $\pm 1.54^\circ$ over the course of the Moon's 346-day draconic year, resulting in distinct seasonal temperature variations at the highest latitudes. The LRO launch date was chosen so that the LRO orbit plane was within 10° of the noon-midnight plane during LRO's first southern summer solstice.
6. Supporting material is available on Science Online.
7. P. O. Hayne *et al.*, *Science* **330**, 477 (2010).
8. R. R. Hodges, *Lunar Planet. Sci. Conf.* **11**, 2463 (1980).
9. D. A. Paige, S. E. Wood, A. R. Vasavada, *Science* **258**, 643 (1992).
10. A. P. Ingersoll *et al.*, *Icarus* **100**, 40 (1992).
11. A. R. Vasavada *et al.*, *Icarus* **141**, 179 (1999).
12. H. Araki *et al.*, *Science* **323**, 897 (2009).
13. M. G. Langseth *et al.*, *Proc. Lunar Sci. Conf.* **7**, 3143 (1976).
14. P. H. Schultz *et al.*, *Science* **330**, 468 (2010).
15. G. J. Taylor *et al.*, *Proceedings of Space Resources Roundtable VI. LPI Contribution No. 1224.*, Golden, CO, Abstract 6040 (Lunar and Planetary Institute, Houston, TX, 2004).
16. N. Schorghofer, G. J. Taylor, *J. Geophys. Res.* **112**, E02010 (2007).
17. We estimate that the total area of surface water ice cold traps in the lunar south polar region shown in Fig. 1D is $13,087 \text{ km}^2$, and the total area of near-surface water ice cold traps to a depth of 1 m is $119,507 \text{ km}^2$.
18. C. J. Hansen, D. A. Paige, *Icarus* **120**, 247 (1996).
19. T. H. Morgan, D. E. Shemansky, *J. Geophys. Res.* **96** (A2), 13511 (1991).
20. D. H. Crider, R. R. Vonrak, *Adv. Space Res.* **31**, 2293 (2003).
21. J. A. Zhang, D. A. Paige, *Geophys. Res. Lett.* **36**, L16203 (2009).
22. J. A. Zhang, D. A. Paige, *Geophys. Res. Lett.* **37**, L03203 (2010).
23. G. R. Gladstone, *Science* **330**, 472 (2010).
24. J. K. Harmon, *Space Sci. Rev.* **132**, 307 (2007).
25. W. C. Feldman *et al.*, *J. Geophys. Res.* **106** (E10), 23,231 (2001).
26. D. J. Lawrence *et al.*, *J. Geophys. Res.* **111**, E08001 (2006).
27. R. C. Elphic *et al.*, *Geophys. Res. Lett.* **34**, L13204 (2007).
28. I. Mitrofanov *et al.*, *Lunar Planet. Sci. Conf.* **41**, 2250 (2010).
29. W. R. Ward, *Science* **189**, 377 (1975).
30. B. G. Bills, R. D. Ray, *Geophys. Res. Lett.* **26**, 3045 (1999).
31. We thank the many people at the Jet Propulsion Laboratory and the Goddard Space Flight Center who contributed to the success of the Diviner instrument and the LRO project. We also thank the National Aeronautics and Space Administration for funding this investigation.

Supporting Online Material

www.sciencemag.org/cgi/content/full/330/6003/479/DC1
Methods
Figs. S1 to S7
References

1 February 2010; accepted 12 August 2010
10.1126/science.1187726

This copy is for your personal, non-commercial use only.

If you wish to distribute this article to others, you can order high-quality copies for your colleagues, clients, or customers by [clicking here](#).

Permission to republish or repurpose articles or portions of articles can be obtained by following the guidelines [here](#).

The following resources related to this article are available online at www.sciencemag.org (this information is current as of October 12, 2015):

Updated information and services, including high-resolution figures, can be found in the online version of this article at:

<http://www.sciencemag.org/content/330/6003/479.full.html>

Supporting Online Material can be found at:

<http://www.sciencemag.org/content/suppl/2010/10/20/330.6003.479.DC1.html>

A list of selected additional articles on the Science Web sites **related to this article** can be found at:

<http://www.sciencemag.org/content/330/6003/479.full.html#related>

This article **cites 23 articles**, 7 of which can be accessed free:

<http://www.sciencemag.org/content/330/6003/479.full.html#ref-list-1>

This article has been **cited by** 14 articles hosted by HighWire Press; see:

<http://www.sciencemag.org/content/330/6003/479.full.html#related-urls>

This article appears in the following **subject collections**:

Planetary Science

http://www.sciencemag.org/cgi/collection/planet_sci